## **ORIGINAL ARTICLE**



# Integrating robotic wire arc additive manufacturing and machining: hybrid WAAM machining

Benquan Li<sup>1</sup> · Kishore M. Nagaraja<sup>1</sup> · Runyu Zhang<sup>1</sup> · Arif Malik<sup>1</sup> · Hongbing Lu<sup>1</sup> · Wei Li<sup>1</sup>

Received: 21 April 2023 / Accepted: 13 October 2023 © The Author(s), under exclusive licence to Springer-Verlag London Ltd., part of Springer Nature 2023

#### Abstract

Wire arc additive manufacturing (WAAM) has received increasing use in 3D printing because of its high deposition rates suitable for components with large and complex geometries. However, the lower forming accuracy of WAAM than other metal additive manufacturing methods has imposed limitations on manufacturing components with high precision. To resolve this issue, we herein implemented the hybrid manufacturing (HM) technique, which integrated WAAM and subtractive manufacturing (via a milling process), to attain high forming accuracy while taking advantage of both WAAM and the milling process. We describe in this paper the design of a robot-based HM platform in which the WAAM and CNC milling are integrated using two robotic arms: one for WAAM and the other for milling immediately following WAAM. The HM was demonstrated with a thin-walled aluminum 5356 component, which was inspected by X-ray micro-computed tomography (µCT) for porosity visualization. The temperature and cutting forces in the component under milling were acquired for analysis. The surface roughness of the aluminum component was measured to assess the surface quality. In addition, tensile specimens were cut from the components using wire electrical discharge machining (WEDM) for mechanical testing. Both machining quality and mechanical properties were found satisfactory; thus the robot-based HM platform was shown to be suitable for manufacturing high-quality aluminum parts.

**Keywords** Hybrid manufacturing · WAAM · Machining · Robots

## 1 Introduction

Hybrid manufacturing (HM) is an emerging technology that combines multiple types of manufacturing technologies. For instance, hybrid additive manufacturing (AM) and conventional subtractive manufacturing in a single fabrication process is a classical hybrid manufacturing [1–4]. HM not only performs 3D printing, but also offers significant improvements to the geometric accuracy and surface quality of printed components via integrated machining operations. Thus, HM has been an attractive technique to both industry and academic research due to its flexibility and high fabrication efficiency. In traditional machining processes, components are typically fabricated by removing material from a workpiece. Although this approach is generally effective, there are certain instances where substantial amounts of

Published online: 24 October 2023



material may be removed during the process. This excess material, if conserved, could find utility in other manufacturing applications (Fig. 1). 3D printing can utilize materials either in powder or wire form, which resolves some of the material waste problems associated with machining [5, 6]. Nevertheless, 3D printing alone is not usually able to make components exactly according to the CAD software models because of the relatively lower fabrication precision when compared to machined parts. Thus, posttreatment processes like milling are commonly adopted for 3D-printed parts to achieve higher accuracy and precision [7]. Therefore, an HM platform equipped with both 3D printing and machining can realize high material utilization rates and competitive surface quality. In a previous study, Li et al. successfully designed and fabricated functionally gradient materials through a customized HM platform that integrated direct energy deposition (DED) and CNC milling machining [8]. Similarly, through an HM technology that converged WAAM and forging operations, Bambach et al. fabricated a jet engine blade with Ti6Al4V by using WAAM in the 3D printing stage and then traditional forging

Wei Li
 Wei.Li@UTDallas.edu

Mechanical Engineering, The University of Texas at Dallas, Richardson, TX, USA

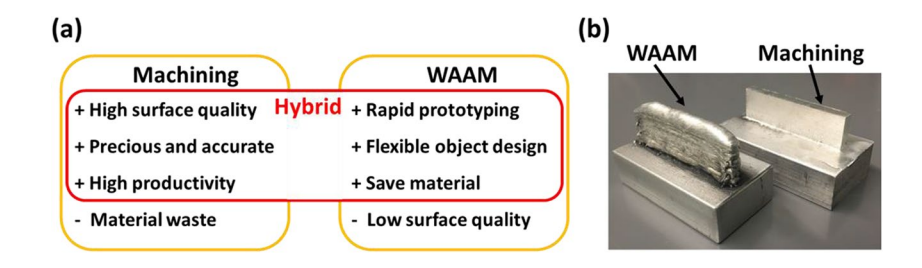
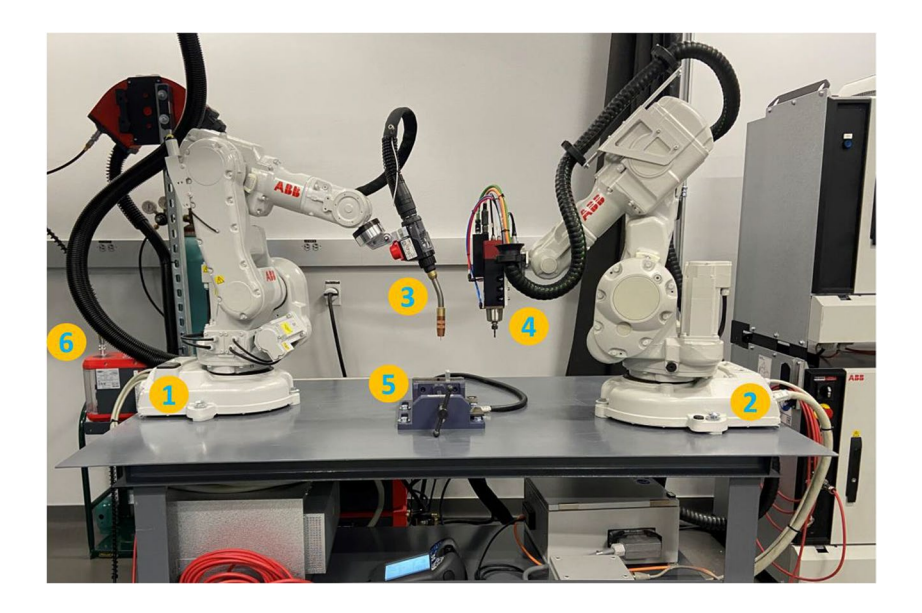


Fig. 1 a The advantages of both AM and subtractive manufacturing, in which hybrid manufacturing technologies converge, are summarized. b The as-built WAAM 3D printed and the machined ones are shown, which reflected the advantages of hybrid manufacturing listed in (a)

processes to obtain the final shape [9]. Du et al. also used HM technology combining selective laser melting (SLM) with precision milling to manufacture an improved surface finish as well as improved geometric and dimensional accuracies of a part. Through a series of experiments, they also showed the good fabrication quality of the HM platform [10]. De Oliveira's team examined how various process parameters, including those in additive manufacturing and post-processing, influenced the surface quality of maraging steel samples, specifically in terms of average roughness and residual stress. The study involved altering the build orientation at three levels in the laser powder bed fusion (LPBF) technique, as well as adjusting the cutting speed and feed per tooth during machining. Furthermore, the study assessed the combined impact of aging heat treatment and milling on surface finishing [11]. Zhang and his group also developed a hybrid additive manufacturing process of stainless steel 316L, combining ultrafast laser machining with laser powder bed fusion (LPBF). By optimizing parameters and alternating LPBF with ultrafast laser machining, they achieved parts with high dimensional accuracy and low surface roughness, addressing critical challenges in LPBF applications [12]. Osman et al. explored heat treatment methods for 18Ni-300 maraging steel produced by additive-subtractive hybrid manufacturing (ASHM). The heat-treated parts showed potential for higher ductility due to increased austenite content (up to 13.4%). The hybrid manufacturing technology with heat treatment proposed in this study suggests that avoiding higher temperatures could maintain comparable mechanical properties while benefiting dimensional stability and surface quality in ASHM [13].

WAAM has been utilized as an AM technology for years, wherein an electric arc functions as the heat source, and metal wires are fed as feedstock materials deposited on a substrate into designed geometries layer by layer along prescribed torch-moving paths. In this paper, a robot-based WAAM was installed as the AM unit in the developed HM platform (Fig. 2). The torch, through which the metal wire was fed, was connected to the positive electrode of the power supply while the substrate was connected to the negative electrode. Generally, in this robot-based gas metal arc welding (GMAW) system, the metal wire is perpendicularly transported to the substrate. As soon as the wire contacts the substrate, it completes a closed circuit. Following this, a

Fig. 2 The customized hybrid manufacturing platform consists of (1) the robotic arm for welding, (2) the robotic arm for milling, (3) the welding torch, (4) a cell spindle and an end mill, (5) bench vice, and (6) welder





robust electric arc melts the wire, forming molten droplets that are deposited onto the substrate (Fig. 3). Subsequently, the deposited part cools naturally in the surrounding air. In this work, compressed argon gas was transferred from a tank to the molten pool at a flow rate of 14.72 l per minute, providing for a shielding environment. In addition, the wire can also be fed or drawn. The flexibility of this robot-based HM platform is also reflected by the 6 degrees of freedom (DOF), which realize complex moving paths when combined with programming. Thus, the moving paths, distances, and speeds cover a vast range. In addition, the welding controller allows a straightforward definition of welding parameters such as voltage, current, and feed rate ranging from 1 to 25 m/min. The welding controller allows for precise adjustment of the welding voltage within a broad range, from 14.2

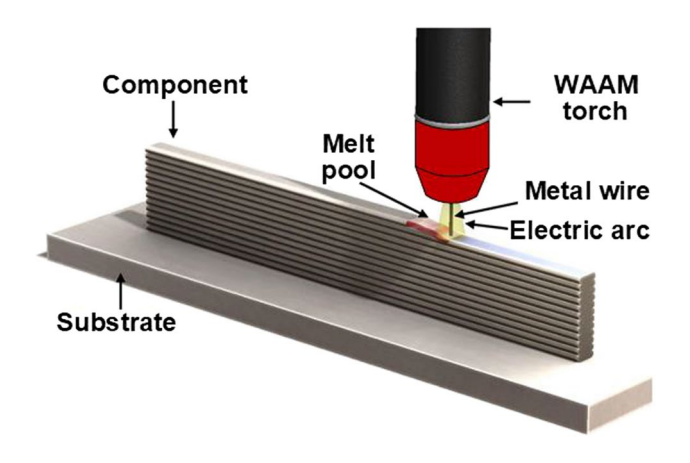


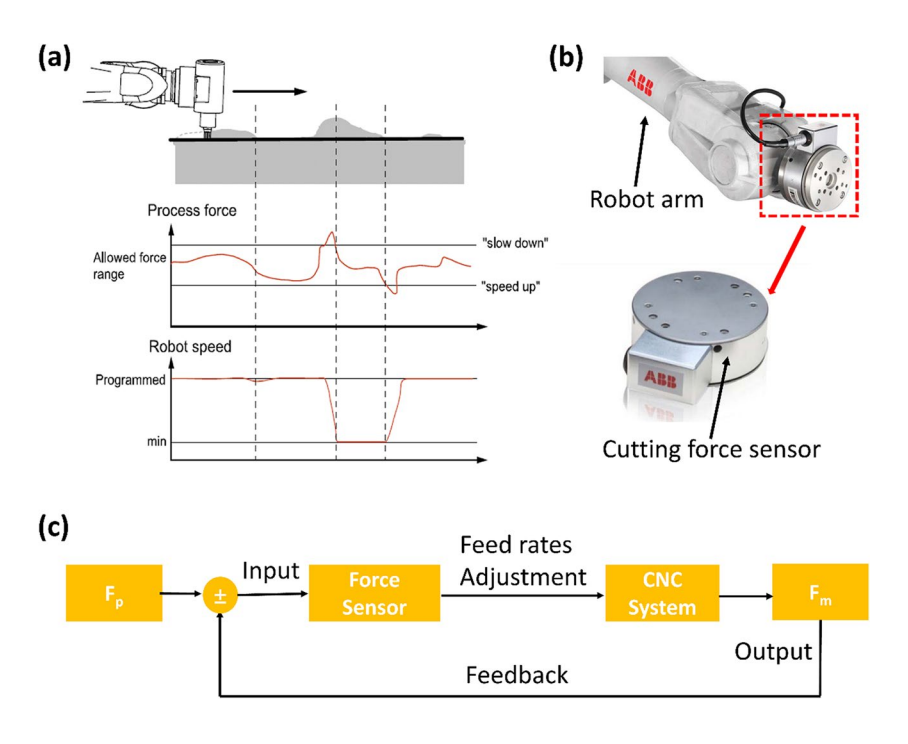
Fig. 3 The operating mechanism of WAAM [14]

Fig. 4 a Illustration of how the cutting forces are kept within a programmed region through adjusting feeding rates. b The cutting force sensor used to detect cutting forces. c The closed-loop control for cutting forces stabilization

to 320 V. Similarly, the welding controller offers an extensive current range, spanning from 3 to 320 A.

The other robotic arm, used for machining, includes an adaptive control system to stabilize the cutting processes and considers that the stiffness of robot-based machine tools is lower than conventional CNC machines. The mechanism of adaptive force control for robotic machining is realized via an ABB force sensor 165 (ABB Robotics, Switzerland) installed between the cell spindle and the end of the robotic arm, as shown in Fig. 4b. The force sensor works to detect the real-time cutting force during machining. The capacity of cutting forces in x, y, and z axes is 165, 165, and 495 N, respectively. The cutting forces are controlled and adjusted by changing the feed rates of the end mill setting in the system controller (Fig. 4a). Before milling operations begin, a specific cutting force value  $(F_n)$  has been programmed in the robotic milling code, which prescribes a threshold to realize stable cutting processes. If there occurs a force measured by the sensor  $(F_m)$  that is lower than the specific  $F_n$ , the robotic arm keeps moving at the defined feed rate in the program. Conversely, if the sensor detects  $F_p < F_m$ , it would reduce the feed rate so that the cutting forces decrease to the specified values. Figure 4c shows the closed-loop control mechanism of this force sensor, in which the cutting forces are detected and delivered as feedback while the feed rates are selected as the input signal that can be adjusted for cutting force stabilization, which is the output.

In this paper, a thin-walled part was manufactured. The component was 3D printed first by one robotic arm.





Then, on the same platform, it was machined by the other robotic arm that was designed to perform CNC milling operations immediately following the 3D printing. During the machining process, cutting temperatures and forces were recorded for further analysis. After machining, the surface roughness was measured for surface quality analysis. Subsequently, dog bone samples were prepared with WEDM for tensile tests. In addition, µCT scan was also conducted to visualize the porosities inside the as-built part to understand the fabrication mechanism of WAAM and also optimize the fabrication quality. Ultimately, it was found that the two-stage hybrid manufacturing processes resulted in excellent fabrication abilities and quality for the described robot-based HM platform, contributing to the innovation and potential application of such manufacturing technologies with high efficiency, flexibility, and quality.

# 2 Experimental procedures

The experiments designed and conducted in this project included fabrication with WAAM, CNC milling machining, and other evaluations to characterize the component manufactured in this HM platform (Fig. 5).

Fig. 5 Setup for welding, milling, and the various tests, depicting the instruments for surface roughness, cutting temperature, cutting forces, internal porosities visualization, and tensile tests

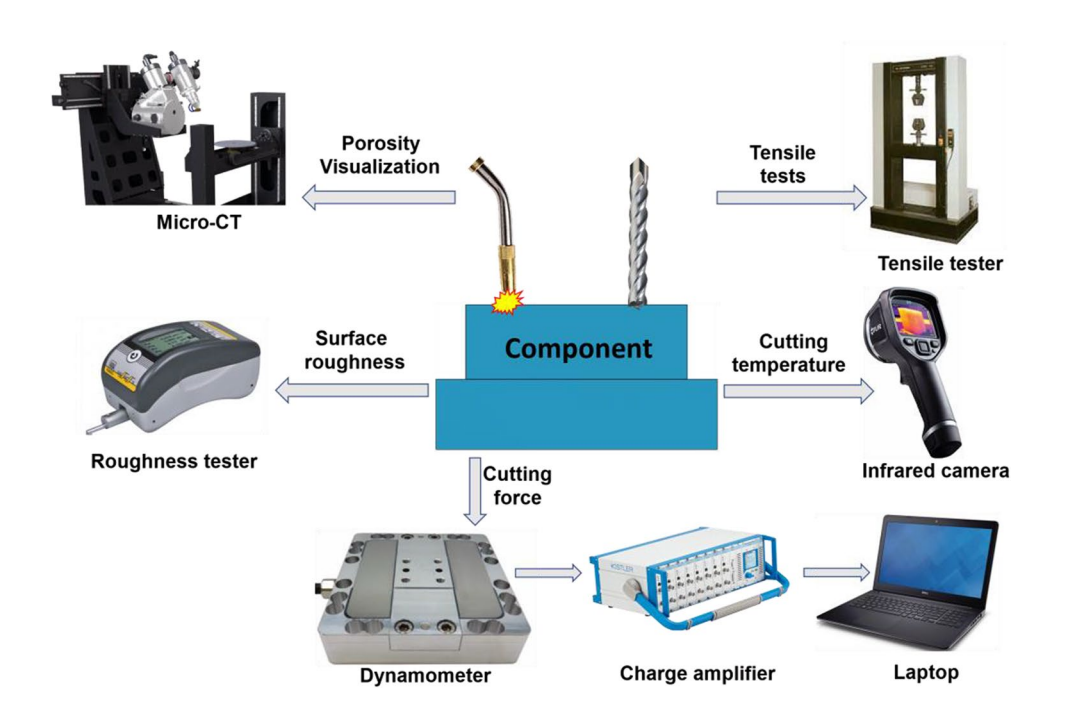


Table 1 Al5356 wire composition (wt.%)

Alloy	Si	Fe	Cu	Mn	Mg	Zn	Al
A15356	0.25	0.4	0.1	0.05-0.2	5.0	0.1	Balance



## 2.1 WAAM process

The deposited material was aluminum 5356 (Al5356), based on the wire diameter of 1 mm. In Table 1, the chemical composition is given [15–17]. Considering that aluminum has a high laser reflection rate, which makes Al additive manufacturing challenging with laser-based equipment, arc usage has been regarded as an optimal alternative heat source for 3D printing of Al [18–20]. The designed model represented a thin-walled part in which 30 layers of single tracks in total were successively built up along the z axis. The printing path for each layer is indicated with red arrows in Fig. 6a which shows the as-built part after WAAM. To make the building process more stable, the single tracks, which were 40 mm long, were printed alternately along both +x and -x directions. A water-cooled welder (Fronius TPS 320i, Fronius International GmbH, Austria), which provided the welding power source, enabled the material deposition process, while the programmed moving paths were executed by the ABB IRB 140 robotic arm (ABB Robotics, Switzerland) on which a welder was assembled. In fact, WAAM is a complex 3D printing technique where a lot of parameters that influence printing quality are involved [1]. To better explain the printing process, all the printing parameters that were optimized values obtained from previous studies were summarized in Table 2.

**Fig. 6** a The designed thin wall model with printing paths in red arrows. b, c The as-built part and the machined part, respectively

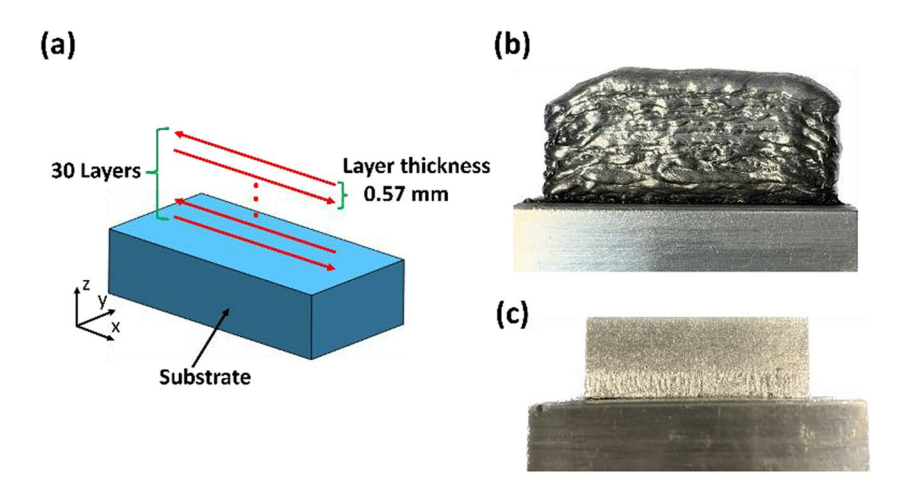
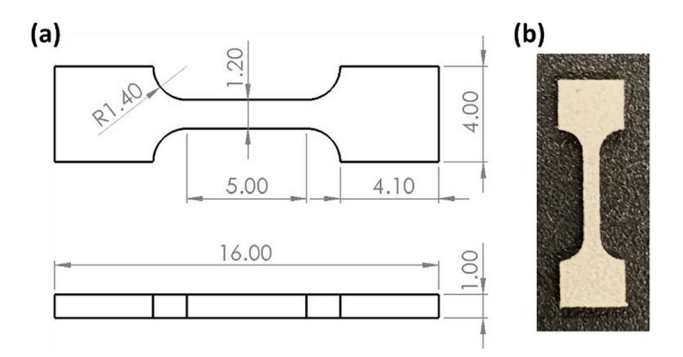


**Table 2** Printing parameters and the values

Parameters	Values/units			
Printing speed	10 mm/s			
Wire feeding rate	335 in/min			
Voltage	17.2 V			
Current	75 A			
Printing direction	$\pm x$ in turn			
Printing layers	30			
Layer thickness	0.57 mm			



2.2 Porosity visualization

As with other AM technologies, the wider applications of WAAM have been limited by the issue of pores and cavities [21, 22] and the lack of an insightful understanding of the porosity mechanism, which is not uncommon in the field of metal 3D printing. Because of the internal porosities, the density of printed parts can be reduced. As a result, mechanical properties such as the tensile strength of the manufactured components can also be impacted. Moreover, porosity is a frequently encountered problem while 3D printing most aluminum alloys, which thus requires researchers to pay greater attention to reducing the porosity as much as possible so that the expected mechanical properties of 3D-printed Al can also be attained [23]. Porosities are generated as a result of the influences from several factors, including arc welding parameters, wire quality, and also shielding gas flow [24-26]. Especially in the fabrication process of a part with multiple layers, the comprehensive influences of the parameters make the porosity mechanism complicated.

In this situation, the investigation of the porosity distribution inside parts made by WAAM is of great significance to demonstrate the fabrication ability of this proposed HM platform and to contribute to the parameter optimizations to manufacture components with better properties in the future. Instead of scaling the mass and measuring the volume of printed parts to calculate the density mathematically,  $\mu$ CT

Fig. 7 The designed model (a) with details of size and a real sample (b) of tested dog bones

scans were performed using an X-ray  $\mu$ CT system (Nikon Metrology Inc.) [27]. The scanning voxel size achieved was 24.97  $\mu$ m. And the porosity formed during the material deposition process was revealed from the reconstructed volumetric images and visualized using a commercial software ORS Dragonfly [40]. The  $\mu$ CT system is shown in Fig. 9.

#### 2.3 Tensile tests

To determine the mechanical properties such as Young's modulus, yield strength, and ultimate strength of a part fabricated by the HM platform, tensile tests were performed for the dog bone samples cut from a manufactured thin-walled part. Tensile tests were performed on an Instron 5567A material test system equipped with a 50 KN load cell. The tested samples, shown in Fig. 7, were prepared with WEDM to have a gauge length of 5 mm and a 1 mm gauge width and thickness. To obtain more accurate data during the tensile tests, the gauge length and cross-sectional area measurements were conducted three times prior to loading. The tensile experiments were carried out at a speed of 0.005 mm/s at room temperature, and the tensile forces and deformation were collected automatically by the Instron machine. Upon



completion of the tests, the stress and strain were computed via the following equations:

$$\sigma = \frac{F}{A_0} \tag{1}$$

$$\varepsilon = \frac{u}{l_0} \tag{2}$$

where  $\sigma$  and  $\varepsilon$  are engineering stress and engineering strain respectively,  $l_0$  and  $A_0$  are the average values of the initial length and the cross-sectional area from multiple measurements, and F and u are the pulling force and displacement of the tested specimens recorded on the testing machine.

Once the engineering strain and engineering stress were calculated, the stress–strain curves were plotted in MAT-LAB to visualize the mechanical properties of the tested samples. Young's modulus (E), yield strength, and ultimate strength are summarized in Table 4. Young's modulus of each sample was calculated using Eq. (3), from the linear elastic region of the stress–strain curves as shown in Fig. 10. To determine more accurate E, the line that best fits these data points within the linear deformation region should be identified. In this project, we employed the least-squares fit technique to calculate the slope of this line, which corresponds to Young's modulus [28].

$$E = \frac{\sigma}{\varepsilon} \tag{3}$$

## 2.4 Milling process

As mentioned previously, post-treatment like machining is necessary to be performed on the AM parts since the rough surface and lower forming precision would impede the direct application of the printed thin wall. The CNC milling unit in this HM platform was specially developed to address the drawbacks of WAAM in terms of poor geometry accuracy. The 3D-printed components were subjected to end milling following the WAAM process without being moved and loaded to a separate CNC machine tool. In addition, the

robot-based milling machine shared the same origin on the same fixture as the other robotic arm for WAAM, which meant the complex calibration steps for both robotic arms were also simplified. In addition, this allowed for machining a printed layer right after the layer was deposited.

Milling operations were carried out using the second ABB IRB 140 robotic arm (ABB Robotics, Switzerland), on which an AF60 CU cell spindle (ELTE, Italy) that connected to an independent CNC system through cables was installed. The milling cutters utilized in this study were tungsten carbide uncoated 4-flute square end mills (MSC Industrial Direct Co., Inc.) with 30° helix-angle and 3/8 inch diameter. The milling scheme conducted is illustrated in Fig. 8a, and the milling parameters are shown in Table 3. To better understand the robotic milling technology capability for parts made by WAAM, as well as to aid in optimizing the milling process for future research, three different feed per tooth values, 3.18, 4.76, 6.35E-3 mm/Z, were selected in the peripheral milling operations, after which machining performance was evaluated. The machined surface was as shown in Fig. 6c. Compared with the as-built part, the machined surface was smooth and bright since the rough surface and the dust caused by welding were removed through the machining operations. In addition, no obvious cracks were observed after milling.

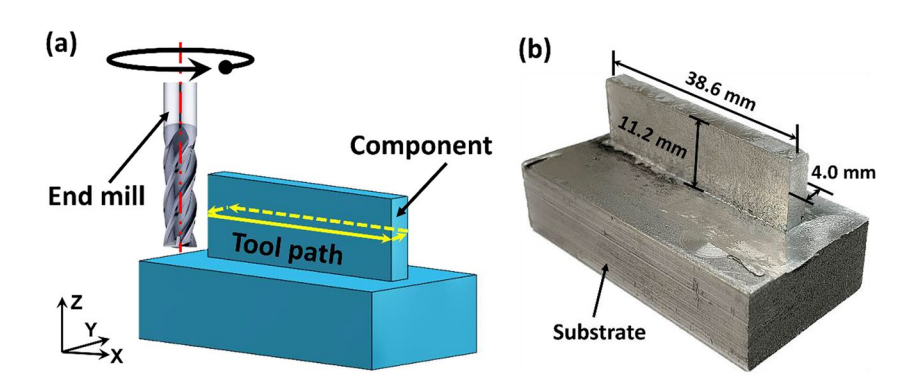
## 2.5 Cutting temperature evaluation

Cutting temperature is another important factor requiring investigation to characterize the performance of this robot-based milling machine in the described HM platform. In this robot-machining process, the machine energy

Table 3 Milling parameters and the values

Cutting parameters (unit)	Value			
Spindle speed (rpm)	1000			
Feed per tooth (mm/Z)	3.18, 4.76, 6.35E-3			
Radial depth of cut (mm)	1			
Axial depth of cut (mm)	2			

Fig. 8 a The profile milling scheme adopted in this study was illustrated, in which the end milling cutter was placed parallel to the workpiece, and the tool path was indicated using the yellow arrows. b After profile milling, the geometry size of the machined part is also shown





generated during the robotic milling was converted to cutting heat through plastic deformation of the metal in the shear zone ahead of the cutting edges, the friction between the cutting tool face and the chip, and the friction between the workpiece and cutting tool [29]. Milling performance is influenced by cutting heat in many aspects. In particular, as the cutting temperature increases during machining, tool strength would decrease, which may cause faster tool wear and even failure. The high temperature realized during machining can also lead to workpiece material adhesion on the cutting tool faces, for which built-up edge tumors might form easily. For Al alloys, which have relatively higher plasticity, built-up edge tumors and other tool wear introduced by high cutting temperatures can also bring about work hardening and residual stresses on the finished surfaces of components, directly affecting the machined surface integrity and the machining precision [30].

To measure the cutting temperature for optimizing the milling operations in this HM platform, an infrared camera FLIR E5-XT (Teledyne Technologies, USA) was utilized to record the temperature changes throughout the machining processes. This was a visual and non-contact temperature measuring tool with a high sensitivity to temperature changes. Before the measurement, the camera was fixed ahead of the bench vice where the thin-walled part was built up and machined. The detector of the infrared camera was focused on the machined regions. Per the milling strategy described earlier, milling operations with three different feeds per tooth were performed, while cutting temperature measurements were also recorded.

## 2.6 Surface roughness measurements

Since the subtractive manufacturing unit was included in this HM platform to make up for the low forming precision of the AM unit, the ability of this machining robotic arm in improving the surface quality of AM parts requires evaluation, particularly since the surface roughness also imposes certain influences on the performance of fabricated parts when they are put into real applications. Accordingly, analyzing the surface roughness of the machined component also helps to optimize the machining parameters so that both the subtractive manufacturing unit and machined parts will function more efficiently and reliably in future studies and manufacturing processes.

In this section, the center line average height  $(R_a)$  of the finished surfaces was measured.  $R_a$  is the arithmetic average of the absolute values of the profile height deviations from the mean line, recorded within the evaluation length. Particularly, the surface roughness  $R_a$  corresponding to the selected three feed per tooth values was measured by a portable roughness tester RUGOSURF 20 (TESA Technology, Switzerland). To obtain more accurate and precise test data, calibration for the tester was

done with a calibration block before the measurement started. To minimize the errors of data,  $R_a$  measurements for each finished surface were repeated multiple times at various locations, while the cutoff length and cutoff number were 0.8 mm and 5, respectively. All the results were recorded and utilized to make boxplots.

#### 2.7 Cutting force measurement

Cutting force is a major factor to be considered in order to achieve high surface quality in milling [31]. The fluctuation of cutting forces needs to be minimized to reach high surface finish quality and long service life of the cutting tool [32]. To investigate the machining performance of this robotic milling tool, the cutting force is a significant parameter that needs to be analyzed. However, the 3D-printed components are different from the wrought ones with regard to their anisotropy in both microstructures and geometries, which makes the machinability of these types of parts unpredictable. As with objects fabricated by the other AM technologies, the WAAM components in this work were not uniform, both in their macro geometries and microstructures. This was attributed to the non-uniform cooling and different thermal histories that consequently induced anisotropies in the distribution of defects and mechanical properties, including hardness, strength, and even residual stress. When 3D-printed parts with significant heterogeneity are machined, the cutting process may show machine chatter and instabilities in cutting forces, chip thickness, and surface quality because of the discontinuities in mechanical properties and surface topography at different positions along the tool moving path [33, 34]. These issues become more serious when machining processes are done by a robot-based machine tool in which the machine stiffness is much lower than with traditional CNC machine tools with solid foundations [35, 36]. Therefore, tool life failure can be accelerated, and satisfying machining quality cannot be ensured. Considering these influences that cutting forces have, a detailed measurement of the cutting forces was conducted for analysis.

Measurements of cutting forces were obtained using a 3-axis force dynamometer, K3D120 (ME-Meßsysteme GmbH, Germany) with a maximum measuring range of  $\pm$  1 KN. This force dynamometer recorded the three component cutting forces in the x, y, and z directions during the machining of specimens printed with WAAM. Then, the active cutting force  $F_a$  was also calculated and analyzed. Milling operations were performed three times using different feeding rates, respectively. The set-up utilized for milling and force measurements is as per the configuration in Fig. 5.



## 3 Results and discussion

# 3.1 Porosity analysis

There are two dominant causes for pore presence in WAAM parts, which are, respectively, the presence of hydrogen and surrounding gas close to the molten pool. In particular, during welding, a continuously increasing amount of hydrogen dissolved in liquid aluminum and surpassed the solubility limit. In this work, as the aluminum rapidly solidified, the excess hydrogen gas bubbles were trapped in the solid aluminum in a homogeneously distributed form. As for the sources of hydrogen, the hydrocarbon contaminants on the surfaces of the wire, water vapor near the arc, and the original hydrogen in the wire likely contributed to the formation of hydrogen bubbles [37]. In addition, the flowing aluminum during welding also traps surrounding air with a rapid solidification rate, and the shielding gas is blown to the molten pool at a certain speed, which was also a main source of porosities inside the components, which usually have inhomogeneous sizes and distribution [38]. From the μCT results presented in Fig. 9b, c, both homogeneously distributed porosities with uniform sizes and randomly distributed porosities with inhomogeneous sizes were observed, caused by both hydrogen gas and surrounding gas (including air and shielding gas). The pores existed in most layers throughout the printed object. In total, the porosities had a volume of up to 9.08 mm<sup>3</sup>, which accounted for 0.126% of the entire volume of the whole fabricated part. As shown in Fig. 9d, most pores were tiny with sphericity close to 1. There only existed a few pores with volumes higher than 0.05 mm<sup>3</sup>. Note that some research groups have been investigating and trying potential creative methods to reduce porosities in WAAM, either through parameter optimizations [22, 26] or other types of post-treatments [37]. Therefore, effective methods that can reduce both kinds of pores should be explored in future projects, which will help improve the manufacturing performance of WAAM in this HM platform.

## 3.2 Mechanical property characterization

The stress-strain curves which reflected the general mechanical properties of the WAAM parts were plotted in MAT-LAB and are presented in Fig. 10. Based on the numerical

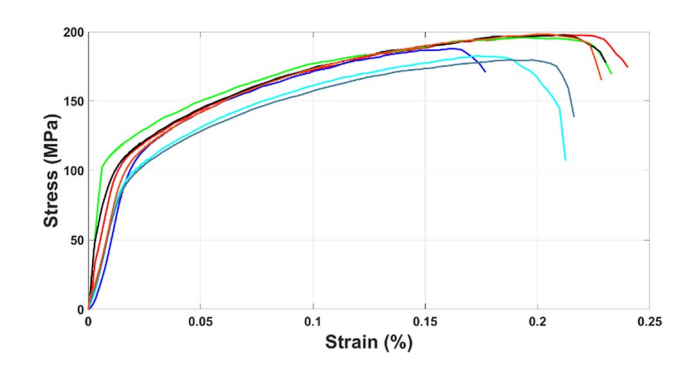
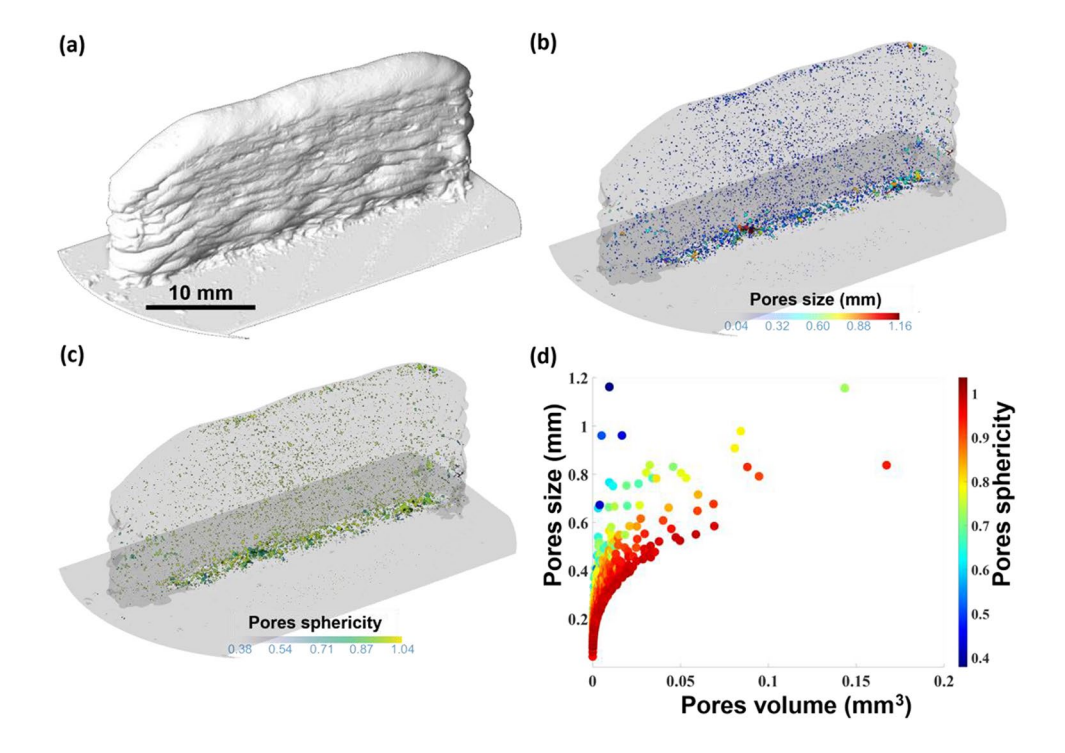


Fig. 10 The stress-strain curves of the dog bone samples EDM cut from the thin-walled specimen manufactured with the HM platform

Fig. 9 Pores distribution inside the thin-walled part revealed by the reconstructed  $\mu$ CT image with a voxel size of 24.97  $\mu$ m and visualized using ORS Dragonfly software. a Scanned view of the part. b, c Pores distribution in 3D view with their size and sphericity indicated by the color bars. d Pores size, volume, and sphericity depicted in a summary graph





data and these curves, Table 4 summarizes the results, including Young's modulus, yield strength, and ultimate strength of the tested samples. All stress-strain curves in this paper were composed of similar sections as the typical curves of wrought aluminum alloys and included linear elastic regions, then strain-hardening regions, and finally necking regions. However, the mechanical properties of each sample did exhibit different values. Some Young's modulus values were higher than 16 GPa. However, some samples only have Young's modulus around 6 GPa. Besides this, obvious differences in yield strength and ultimate strength were also observed, although all the samples were prepared from the same thin-walled part. These value variations of mechanical properties might be attributed to the nonuniform distribution of flaws and defects like pores in the samples. These defects could not only introduce stress concentration, making the samples fail earlier than the other samples with less flaws, but also occur unpredictably at random locations on 3D-printed components. Thus, reducing defects and technology optimizations to fabricate parts with higher and more stable mechanical properties should be a significant focus in the following studies of the HM platform.

# 3.3 Cutting temperature analysis

Next, the cutting temperature from each milling trial was extracted and plotted using MATLAB (Fig. 11). It was shown that the cutting temperature in each milling operation increased rapidly from room temperature as the thin-walled part was machined. Then, the cutting temperature reached

an equilibrium until the end of machining, which was followed by a natural temperature decrease. To be specific, once the rotating end mill contacted the part to be machined, a considerable amount of machine energy was converted to cutting heat, leading to a sharp temperature rise. Subsequently, as the most of machining heat was transferred to the detached chips, which were removed from finished surfaces, and some remaining heat was dissipated to the surrounding air, the cutting temperature reached an equilibrium state.

Since the feed per tooth was different in each cutting round, total cutting time also varied, although the cutting distance was the same value, 38 mm. When the higher feed per tooth was selected, more energy was consumed to overcome the friction and remove the materials per unit of time, which generated more heat increasing the cutting temperature. Thus, the cutting temperature of the milling trial in a feed per tooth of 3.18E-3 mm/Z was lower overall than the other two milling trials in which higher feed per tooth of 4.76 and 6.35E-3 mm/Z was used. The slight variation in each curve was introduced by the rough surfaces of as-built parts after WAAM. The rough surfaces with lower geometry precision made the real cutting depth during machining either higher or lower than the input value in the machining program.

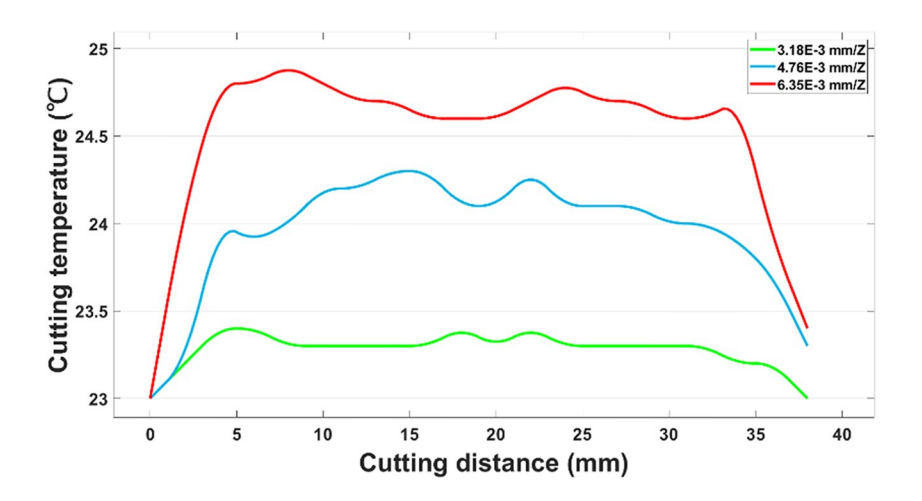
# 3.4 Surface roughness analysis

The surface roughness values of three finished surfaces were processed with MATLAB and given in the boxplots of Fig. 12. 3D-printed metal components can exhibit varying

Table 4 Results of tensile tests

Samples	No. 1	No. 2	No. 3	No. 4	No. 5	No. 6	No. 7
Elastic modulus (GPa)	8.82	16.30	5.12	5.93	13.76	5.72	6.33
Yield strength (MPa)	112.6	109.6	109.0	101.3	109.5	98.1	110.5
Ultimate strength (MPa)	197.8	195.9	187.8	182.5	197.5	179.6	198.1

Fig. 11 Cutting temperature history of three milling trials with feed per tooth of 3.18E-3, 4.76E-3, and 6.35E-3 mm/Z





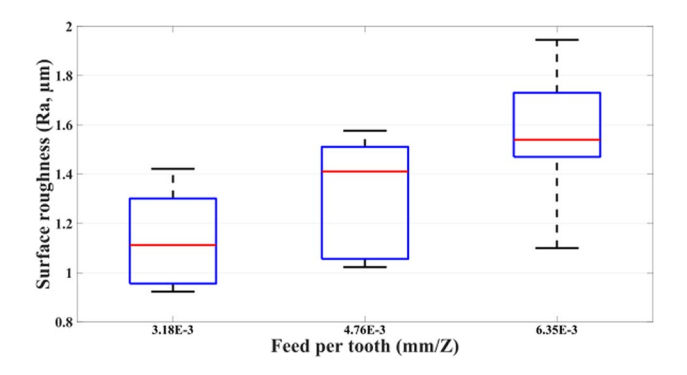


Fig. 12 Plot showing that, after machining, the surface roughness of printed thin-walled part also varied as a result of different feed per tooth used

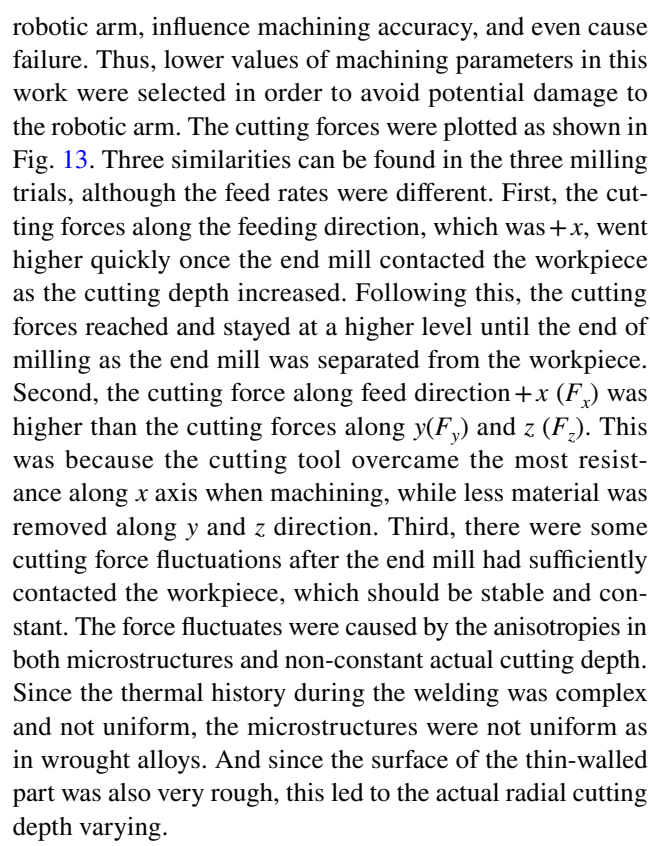
mechanical properties at different locations due to the complex thermal history during printing. Therefore, surface roughness after cutting may not necessarily follow the same trends as wrought metal materials due to the non-uniformly distributed material properties. This underscores the importance of investigating the surface roughness of parts fabricated with WAAM.

The tendency of  $R_a$  changes could be observed in the results, which was that  $R_a$  would be higher as the feed rate increased. When the feed per tooth was 3.18E-3 mm/Z, the average  $R_a$  value was about 1.1 µm, while the average  $R_a$  could reach about 1.4 and even 1.54 µm as the feed per tooth was increased to 4.76 and 6.35E-3 mm/Z, respectively. In particular, the increase of feed per tooth could be understood as more material was removed per unit of time, which meant the load on the robotic arm and also the reaction forces on the workpiece tended to increase. Under this circumstance, aluminum with higher plasticity was deformed more because of the higher feed rate, which consequently increased the surface roughness on the machined surfaces.

This change in the  $R_a$  value with varying feed per tooth aligns with findings from previous milling studies with aluminum alloys [39]. This suggests that the milling performance of this robotic machining tool can be considered typical in terms of surface quality control, relative to other traditional CNC machines. Furthermore, this evolution of  $R_a$  indicates that the 3D-printed metal part exhibited relatively consistent material properties across different locations on the machined part, underscoring the expected fabrication stability of this WAAM device.

## 3.5 Cutting force analysis

For robot-based machine tools, relatively lower machine stiffness makes the cutting force a crucial factor that cannot be ignored. Too much force load would damage the



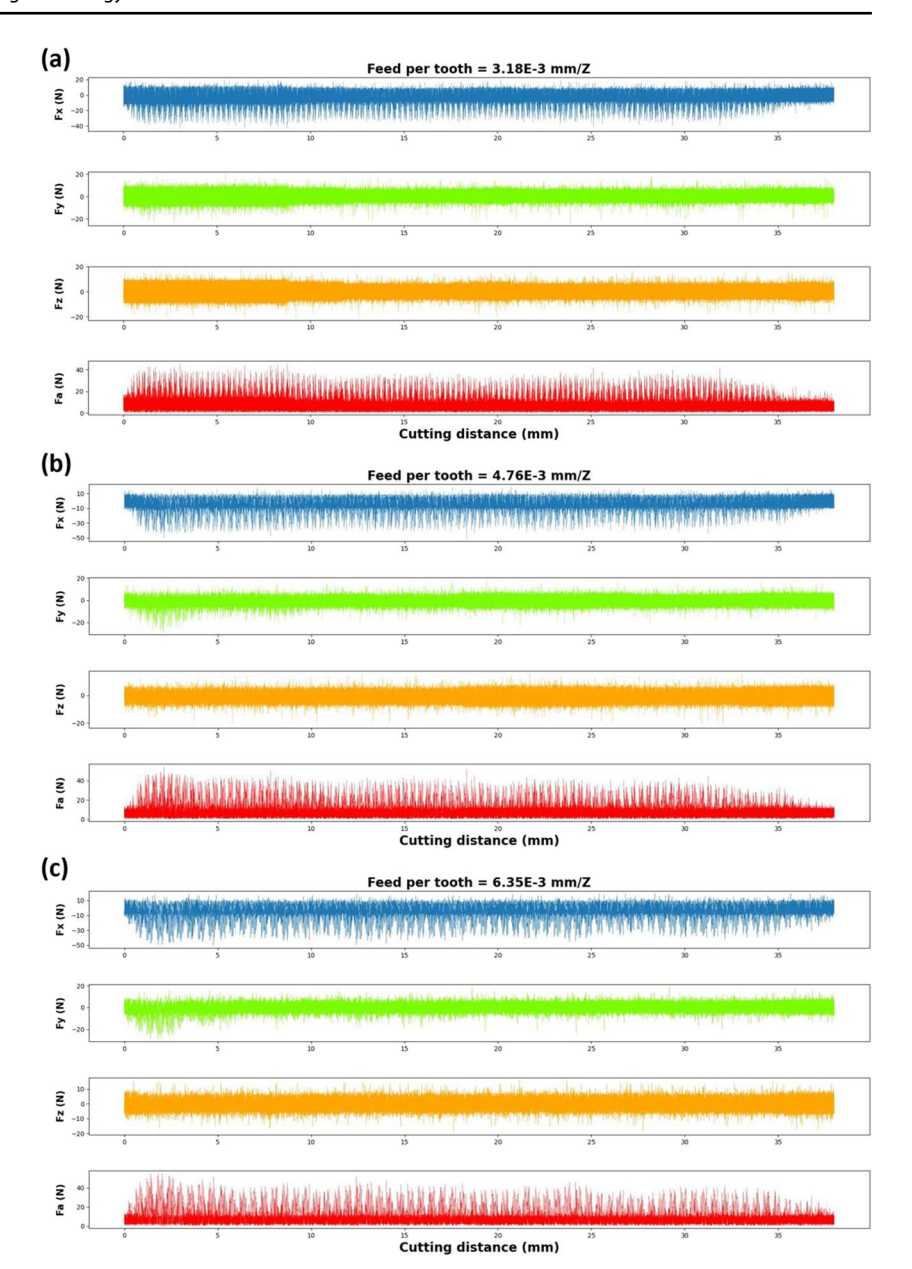
Apart from the similarities, the difference among the three plots was that the main cutting force tended to be higher as the feed per tooth improved, which is a straightforward rule in the machining field. The maximum cutting forces,  $F_{\rm r}$ , in the three milling trials, were – 42.6, – 50.2, and -50.7 N, as feed per tooth varied from 3.18E-3, 4.76E-3, and 6.35E-3 mm/Z. Such a tendency can also be applied to  $F_a$ . Since the material to be removed per unit of time increased, the forces that the robotic arm provided were expected to increase. In a manner consistent with our examination of surface roughness, the analysis of cutting forces in WAAMed components revealed a conventional trend overall. This trend suggests that the special material properties of 3D-printed components do not significantly impact cutting performance. Drawing this conclusion holds particular importance as it provides valuable insights for the design of manufacturing processes involving WAAMed components in future industrial scenarios.

# 4 Conclusion

In this paper, a customized robot-based hybrid manufacturing platform, which integrates both additive manufacturing (AM) and subtractive manufacturing, was introduced. The AM unit, realized through wire arc additive manufacturing (WAAM), effectively 3D prints the designed geometries.



Fig. 13 The cutting force and related active force results collected from three milling trials with feed per tooth of 3.18E-3, 4.76E-3, and 6.35E-3 mm/Z respectively



Milling machining was equipped as the subtractive manufacturing unit to perform post-treatments and improve the fabrication accuracy and precision of the 3D-printed objects. Through a series of experiments and tests on porosities, surface roughness, cutting temperature, cutting forces, and mechanical properties, the following conclusions can be drawn:

- The HM platform is able to fabricate designed models, taking full advantage of both WAAM and milling to print and then machine the components.
- · Porosity is an inevitable issue in WAAM and can negatively influence mechanical properties such as Young's modulus, Yield strength, and Ultimate strength, which was revealed in the stress-strain curves obtained from

tensile tests. However, porosity ratios can be decreased through parameter optimizations and other types of post-treatments.

The anticipated machining performance of the robot-based milling tool was indeed demonstrated, notably showcased by the significantly improved surface quality post-milling. Despite potential variations in material properties between WAAMed components and traditional wrought metal materials, the findings pertaining to surface roughness, cutting temperature, and cutting forces conformed to established machining principles, particularly in response to changes in feed per tooth. This alignment underscores the WAAM device's capability to manufacture metal parts with relatively consistent material properties.



**Funding** Li acknowledges the support of STARS funding from Texas. Lu thanks the support of NSF under 2219347, the Department of Energy under DE-NA0003962 & DE-NA-0003525, and the Louis A. Beecherl Jr. endowed chair.

**Data availability** Since the data is part of an ongoing study, it cannot be shared to reproduce the results.

Code availability Not applicable.

## **Declarations**

Ethics approval Not applicable.

Consent to participate Not applicable.

**Consent for publication** The authors have agreed and provided consent for the published version of the manuscript.

**Competing interests** The authors declare no competing interests.

## References

- Rodrigues TA, Duarte V, Miranda RM et al (2019) Current status and perspectives on wire and arc additive manufacturing (WAAM). Materials 12:1121. https://doi.org/10.3390/ma12071121
- Strong D, Kay M, Conner B et al (2018) Hybrid manufacturing integrating traditional manufacturers with additive manufacturing (AM) supply chain. Addit Manuf 21:159–173. https://doi.org/10. 1016/j.addma.2018.03.010
- Korkmaz ME, Waqar S, Garcia-Collado A et al (2022) A technical overview of metallic parts in hybrid additive manufacturing industry. J Market Res 18:384–395. https://doi.org/10.1016/j.jmrt. 2022.02.085
- Li W, Amanov A, Nagaraja KM et al (2023) Processing aluminum alloy with hybrid wire arc additive manufacturing and ultrasonic nanocrystalline surface modification to improve porosity, surface finish, and hardness. J Manuf Process 103:181–192. https://doi. org/10.1016/j.jmapro.2023.08.047
- Chen L, Lau TY, Tang K (2020) Manufacturability analysis and process planning for additive and subtractive hybrid manufacturing of quasi-rotational parts with columnar features. Comput Aided Des 118:102759. https://doi.org/10.1016/j.cad.2019.102759
- Lorenz KA, Jones JB, Wimpenny DI, Jackson MR (2015) A review of hybrid manufacturing. 2014 International Solid Freeform Fabrication Symposium, Austin
- Petrick IJ, Simpson TW (2013) 3D printing disrupts manufacturing: how economies of one create new rules of competition. Res Technol Manag 56:12–16. https://doi.org/10.5437/08956308X5606193
- Li B, Zhang R, Malik A, Li W (2022) Machinability of partition milling stainless steel/Inconel functionally gradient material printed with directed energy deposition. Int J Adv Manuf Technol 122:3009–3022. https://doi.org/10.1007/s00170-022-10111-8
- Bambach M, Sizova I, Sydow B et al (2020) Hybrid manufacturing of components from Ti-6Al-4V by metal forming and wirearc additive manufacturing. J Mater Process Technol 282:116689. https://doi.org/10.1016/j.jmatprotec.2020.116689
- Du W, Bai Q, Zhang B (2016) A novel method for additive/subtractive hybrid manufacturing of metallic parts. Procedia Manuf 5:1018–1030. https://doi.org/10.1016/j.promfg.2016.08.067
- De Oliveira AR, Del Conte EG (2021) Concurrent improvement of surface roughness and residual stress of as-built and aged additively manufactured maraging steel post-processed by

- milling. Int J Adv Manuf Technol 116:2309–2323. https://doi.org/10.1007/s00170-021-07527-z
- 12. Zheng B, Trofimov V, Yang Y et al (2023) Study on additive and subtractive manufacturing of high-quality surface parts enabled by picosecond laser. J Mater Process Technol 318:118013. https://doi.org/10.1016/j.jmatprotec.2023.118013
- Osman M, Sarafan S, Wanjara P et al (2023) Effect of heat treatment on the microstructure and mechanical properties of 18Ni-300 maraging steel produced by additive-subtractive hybrid manufacturing. Materials 16:4749. https://doi.org/10. 3390/ma16134749
- McAndrew AR, Alvarez Rosales M, Colegrove PA et al (2018) Interpass rolling of Ti-6Al-4V wire + arc additively manufactured features for microstructural refinement. Addit Manuf 21:340–349. https://doi.org/10.1016/j.addma.2018.03.006
- Ouyang JH, Wang H, Kovacevic R (2002) Rapid prototyping of 5356-aluminum alloy based on variable polarity gas tungsten arc welding: process control and microstructure. Mater Manuf Processes 17:103–124. https://doi.org/10.1081/AMP-120002801
- Wang L, Suo Y, Liang Z et al (2019) Effect of titanium powder on microstructure and mechanical properties of wire + arc additively manufactured Al-Mg alloy. Mater Lett 241:231–234. https://doi. org/10.1016/j.matlet.2019.01.117
- Jiangang P, Bo Y, Jinguo G et al (2022) Influence of arc mode on the microstructure and mechanical properties of 5356 aluminum alloy fabricated by wire arc additive manufacturing. J Market Res 20:1893–1907. https://doi.org/10.1016/j.jmrt.2022.08.005
- Zhang J, Song B, Wei Q et al (2019) A review of selective laser melting of aluminum alloys: processing, microstructure, property and developing trends. J Mater Sci Technol 35:270–284. https:// doi.org/10.1016/j.jmst.2018.09.004
- Wang A, Wang H, Wu Y, Wang H (2021) 3D printing of aluminum alloys using laser powder deposition: a review. Int J Adv Manuf Technol 116:1–37. https://doi.org/10.1007/s00170-021-07440-5
- Naeem M (2013) Laser processing of reflective materials: a new technology managing reflection effects. LTJ 10:18–20. https://doi. org/10.1002/latj.201390001
- Horgar A, Fostervoll H, Nyhus B et al (2018) Additive manufacturing using WAAM with AA5183 wire. J Mater Process Technol 259:68–74. https://doi.org/10.1016/j.jmatprotec.2018.04.014
- Ryan EM, Sabin TJ, Watts JF, Whiting MJ (2018) The influence of build parameters and wire batch on porosity of wire and arc additive manufactured aluminium alloy 2319. J Mater Process Technol 262:577–584. https://doi.org/10.1016/j.jmatprotec.2018.07.030
- Hauser T, Reisch RT, Breese PP et al (2021) Porosity in wire arc additive manufacturing of aluminium alloys. Addit Manuf 41:101993. https://doi.org/10.1016/j.addma.2021.101993
- Williams SW, Martina F, Addison AC et al (2016) Wire + arc additive manufacturing. Mater Sci Technol 32:641–647. https:// doi.org/10.1179/1743284715Y.0000000073
- Singh SR, Khanna P (2021) Wire arc additive manufacturing (WAAM): a new process to shape engineering materials. Mater Today: Proc 44:118–128. https://doi.org/10.1016/j.matpr.2020.08.030
- Arana M, Ukar E, Rodriguez I et al (2021) Strategies to reduce porosity in Al-Mg WAAM parts and their impact on mechanical properties. Metals 11:524. https://doi.org/10.3390/met11030524
- 27. Amirkhizi A, Furmanski J, Franck C et al (2023) Challenges in mechanics of time-dependent materials & mechanics of biological systems and materials, volume 2: Proceedings of the 2022 Annual Conference on Experimental and Applied Mechanics. Springer International Publishing, Cham
- Wachtman JB, Tefft WE, Lam DG, Apstein CS (1961) Exponential temperature dependence of Young's modulus for several oxides. Phys Rev 122:1754–1759. https://doi.org/10.1103/PhysRev.122.1754
- 29. Sun Y, Sun J, Li J, Xiong Q (2014) An experimental investigation of the influence of cutting parameters on cutting temperature



- in milling Ti6Al4V by applying semi-artificial thermocouple. Int J Adv Manuf Technol 70:765–773. https://doi.org/10.1007/s00170-013-5294-1
- 30. Longbottom JM, Lanham JD (2005) Cutting temperature measurement while machining a review. Aircr Eng Aerosp Technol 77:122–130. https://doi.org/10.1108/00022660510585956
- Qiao G, Zhang B, Bai Q et al (2022) Machinability of TiC-reinforced titanium matrix composites fabricated by additive manufacturing. J Manuf Process 76:412–418. https://doi.org/10.1016/j.jmapro.2022.02.033
- 32. Suresh Kumar Reddy N, Venkateswara Rao P (2006) Experimental investigation to study the effect of solid lubricants on cutting forces and surface quality in end milling. Int J Mach Tools Manuf 46:189–198. https://doi.org/10.1016/j.ijmachtools. 2005.04.008
- Oyelola O, Jackson-Crisp A, Crawforth P et al (2020) Machining of directed energy deposited Ti6Al4V using adaptive control. J Manuf Process 54:240–250. https://doi.org/10.1016/j.jmapro.2020.03.004
- Lizzul L, Sorgato M, Bertolini R et al (2020) Influence of additive manufacturing-induced anisotropy on tool wear in end milling of Ti6Al4V. Tribol Int 146:106200. https://doi.org/10.1016/j.tribo int.2020.106200
- Wang J, Zhang H, Fuhlbrigge T (2009) Improving machining accuracy with robot deformation compensation. In: 2009 IEEE/ RSJ International Conference on Intelligent Robots and Systems. IEEE, St. Louis, MO, USA, pp 3826–3831
- Zhang X, Yang W, Cheng X, Chen Y (2011) Stiffness identification for serial robot manipulator based on uncertainty approach.
  In: Jeschke S, Liu H, Schilberg D (eds) Intelligent Robotics and

- Applications. Springer, Berlin Heidelberg, Berlin, Heidelberg, pp 378-388
- Gu J, Ding J, Williams SW et al (2016) The effect of inter-layer cold working and post-deposition heat treatment on porosity in additively manufactured aluminum alloys. J Mater Process Technol 230:26–34. https://doi.org/10.1016/j.jmatprotec.2015.11.006
- Gu JL, Ding JL, Cong BQ et al (2014) The influence of wire properties on the quality and performance of wire+arc additive manufactured aluminium parts. AMR 1081:210–214. https://doi. org/10.4028/www.scientific.net/AMR.1081.210
- Kiswanto G, Zariatin DL, Ko TJ (2014) The effect of spindle speed, feed-rate and machining time to the surface roughness and burr formation of aluminum alloy 1100 in micro-milling operation. J Manuf Process 16:435–450. https://doi.org/10.1016/j. jmapro.2014.05.003
- Dragonfly 2020.2 [Computer software]. Object research systems (ORS) Inc, Montreal, Canada, 2020; software available at http://www.theobjects.com/dragonfly

**Publisher's Note** Springer Nature remains neutral with regard to jurisdictional claims in published maps and institutional affiliations.

Springer Nature or its licensor (e.g. a society or other partner) holds exclusive rights to this article under a publishing agreement with the author(s) or other rightsholder(s); author self-archiving of the accepted manuscript version of this article is solely governed by the terms of such publishing agreement and applicable law.

